Effective slip boundary conditions for sinusoidally corrugated surfaces

Lin Guo,[1] Shiyi Chen,[1,2] and Mark O. Robbins[1,3,*]

[1]*Department of Mechanical Engineering, Johns Hopkins University, Baltimore, Maryland 21218, USA*
[2]*South University of Science and Technology, Shenzhen, Guangdong 518055, China*
[3]*Department of Physics and Astronomy, Johns Hopkins University, Baltimore, Maryland 21218, USA*

Molecular dynamics simulations are used to investigate the effective slip boundary condition for a simple fluid flowing over surfaces with one-dimensional sinusoidal roughness in the Wenzel state. The effective slip length is calculated as a function of the corrugation amplitude for flows along two principal orientations: transverse and longitudinal to the corrugation. Different atomic configurations, bent and stepped, are examined for strong and weak wall-fluid interactions and high and low wall densities. Molecular dynamics results for sparse bent surfaces quantitatively agree with continuum hydrodynamic predictions with a constant local slip length. Increasing the roughness amplitude reduces the effective slip length and the reduction is larger for transverse flow than longitudinal flow. Atomic effects become important for dense surfaces, because the local slip length varies with the local curvature and atomic spacing along the wall. These effects can be captured by applying a spatially varying boundary condition to the Navier-Stokes equations. Results for stepped surfaces are qualitatively different than continuum predictions, with the effect of corrugation rising linearly with corrugation amplitude rather than quadratically. There is an increased drag for transverse flow that is proportional to the density of step edges and lowers the slip length. Edges tend to increase the slip length for longitudinal flow because of order induced along the edges.

I. INTRODUCTION

Progress in the design and fabrication of micro- and nanofluidic devices has raised the importance of precisely modeling the transport properties of fluids near solid surfaces. Conventional continuum hydrodynamics treats interfacial effects as boundary conditions applied to mathematically sharp interfaces. As the system size shrinks to micro- or nanoscales, the classical no-slip boundary condition for macroscopic hydrodynamics may be violated and fluid flow can be substantially modified by fluid slip at the solid surface [1–5].

Navier proposed a widely used slip boundary condition for flat and homogeneous surfaces [6], which postulates that the slip velocity is proportional to the shear rate of the fluid at the surface. The slip length (also referred to as intrinsic slip length) is introduced as the proportionality coefficient and is used to characterize the degree of slip. Previous molecular dynamics studies [7–14] have reported that, at small shear rates, the slip length is determined by the properties of the fluid (e.g., viscosity, temperature, and fluid structure) and the atomic-scale properties of the interface (e.g., wall-fluid interaction strength and atomic structure of the surface).

In most real systems, the solid surfaces are rough at small scales. To describe the bulk fluid flow away from the surface, it is appropriate to define an effective Navier slip boundary condition to account for the mean effects of the variations in height and local wall-fluid coupling along the real surface [15–21]. The effective slip length measures the distance from the location of the mean height of the surface to the virtual plane where the extrapolated velocity from the bulk flow profile coincides with that of the solid wall. A larger (more positive) effective slip length indicates a smaller effective drag coefficient between the fluid and wall.

---

*mr@jhu.edu

Because of the potential applications, especially in drag reduction and flow control, the effects of surface roughness have been extensively studied by means of experiments, simulations, and theory. Usually, wall roughness decreases the degree of effective slip [15,17,18,22–28]. However, it is well known that highly hydrophobic rough surfaces may trap gas bubbles in the valleys and form a Cassie state, which can dramatically enhance the effective slip [20,29–41]. In contrast to the conventional point of view, it has also been reported that roughness may generate very large effective slip even in the Wenzel state, where there is no gas trapped in valleys [42,43]. If the corrugations on the surface are anisotropic, then the effective slip length becomes anisotropic too [39,44–51].

The above work clearly shows that surface roughness can significantly affect the effective wall-fluid coupling. However, the mechanisms involved are not yet fully understood, due to the complex interplay of the various atomic and continuum effects associated with the wide range of roughness length scales.

In this study we use molecular dynamics (MD) simulations to investigate the anisotropic slip of Newtonian monatomic fluids over surfaces with one-dimensional sinusoidal roughness in the Wenzel state. Different types of corrugated surfaces are compared: smoothly bent surfaces where atoms of a crystalline solid are displaced to follow a sine wave and stepped surfaces that are cut from a crystalline solid. The wavelength is always more than an order of magnitude larger than the atomic diameter, so effects from atomic discreteness can be separated from those of the large-scale corrugations. The wall density and the wall-fluid interaction are varied.

The effective slip length is calculated as a function of the corrugation amplitude for flows along two principal orientations: transverse and longitudinal to the corrugation. Molecular dynamics results for low-density (sparse) bent surfaces quantitatively agree with continuum hydrodynamic predictions with a constant local boundary condition. The effective slip length decreases monotonically with increasing corrugation amplitude and the reduction is larger for transverse flow than longitudinal flow. Atomic effects become important for close-packed (dense) bent surfaces. Curvature at the crests of dense rough surfaces produces large variations in the local slip length [52]. The resulting changes in total effective slip length are captured by supplementing continuum simulations with local slip boundary conditions obtained for the corresponding curvature and atomic spacing.

Results for stepped surfaces are qualitatively different than continuum predictions. Steps introduce an extra drag for transverse flow that has no analog in continuum theory and has pronounced effects when there is significant slip on flat surfaces. In particular, the analytic scaling at small amplitudes changes from quadratic to linear in the roughness amplitude. This shows that the transverse drag is proportional to the density of step edges. The slip length for longitudinal flow also scales with the density of step edges, but tends to increase with roughness rather than decreasing.

The rest of the paper is organized as follows. In Sec. II we describe the details of molecular dynamics and continuum simulations and how key quantities such as slip length and fluid structure are defined and measured from the simulations. In Sec. III results for the effective slip length are presented and the effect of wall roughness is discussed. A summary and conclusions are given in Sec. IV.

II. SIMULATION METHODS AND ANALYTICAL MODELS

A. Molecular dynamics simulations

Standard molecular dynamics is used to simulate simple fluid flows over rigid solid walls. The simulations are performed with the open source package LAMMPS from Sandia National Laboratories [53]. A truncated Lennard-Jones (LJ) potential is used to model the interactions between fluid atoms

$$V_{\text{LJ}}(r) = 4\epsilon \left[\left(\frac{\sigma}{r} \right)^{12} - \left(\frac{\sigma}{r} \right)^{6} \right] - V_c \quad \text{for } r < r_c, \tag{1}$$

where r is the distance between the two atoms and ϵ and σ define the characteristic energy and length scales of the fluid, respectively. To save computational cost, V_{LJ} is truncated at a distance
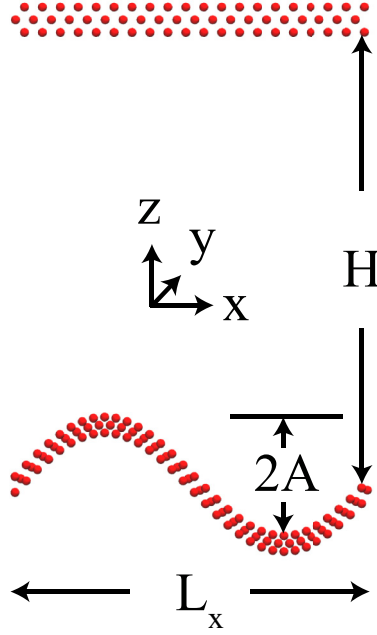
FIG. 1. Geometry of the MD simulation. Fluid is confined between rigid walls. The bottom wall has a sinusoidal corrugation $z(x) = A\sin(2\pi x/\lambda_x)$ with mean height zero. The surface of the flat top wall is placed at $z = H$ and a no-slip boundary condition is enforced there by choosing a strong wall-fluid interaction. Flow is generated by moving the top wall along either the x or the y axis.

$r_c = 2.2\sigma$ and V_c is chosen so that $V_{\mathrm{LJ}}(r_c) = 0$. Wall (w) and fluid (f) atoms also interact through a truncated LJ potential with parameters ϵ_{wf} and σ_{wf} and the same cutoff distance $r_{c,wf} = 2.2\sigma$.

The equations of motion are integrated using the velocity-Verlet algorithm with a time step $\Delta t = 0.005\tau$, where $\tau = \sigma\sqrt{m/\epsilon}$ is the characteristic time scale and m is the mass of a fluid atom. Fluid temperature is maintained at $T = 1.1\epsilon/k_B$ by imposing a Langevin thermostat on all fluid atoms in a direction perpendicular to the bulk flow and flow gradient. For example, for flows along the x (y) direction and walls separated in the z direction, the Langevin thermostat is applied in the y (x) direction (Fig. 1) [7,54]. The thermostated equation of motion in the y direction is given by

$$m\ddot{y} = f_{\mathrm{LJ}} - m\Gamma\dot{y} + F(t), \tag{2}$$

where f_{LJ} is the total LJ force from all other particles. The damping rate Γ controls the heat flux between the system and the heat bath and $F(t)$ is a random force sampled from a Gaussian distribution with zero mean and variance $2m\Gamma k_B T/\Delta t$. We use a damping rate $\Gamma = 0.5\tau^{-1}$, which effectively eliminates viscous heating without causing any substantial disturbances to the atomic motions. In this regime of low damping rate, the thermostat has negligible impact on the effective slip boundary condition on flat surfaces [7,55,56]. We confirmed that this remains true even for y direction flows, where weak secondary momentum transfer can occur along the thermostated x direction. In particular, varying Γ by a factor of 2 or switching to an isotropic momentum-conserving dissipative particle dynamics thermostat [57–59] with a damping rate $0.5\tau^{-1}$ had negligible impact on the effective slip length ($<3\%$).

The density of the bulk fluid is fixed at $\rho = 0.81\sigma^{-3}$. For the low-shear-rate regime studied here ($<0.04\tau^{-1}$), the bulk fluid is Newtonian with shear viscosity $\mu \sim 2.13\epsilon\tau\sigma^{-3}$. We verified that the slip length is insensitive to shear rate in this regime [7,8,12,17,56].

As illustrated in (Fig. 1), fluid is confined in a channel between two solid walls. Periodic boundary conditions are imposed along the x and y directions with the spatial periods denoted by L_x and L_y,
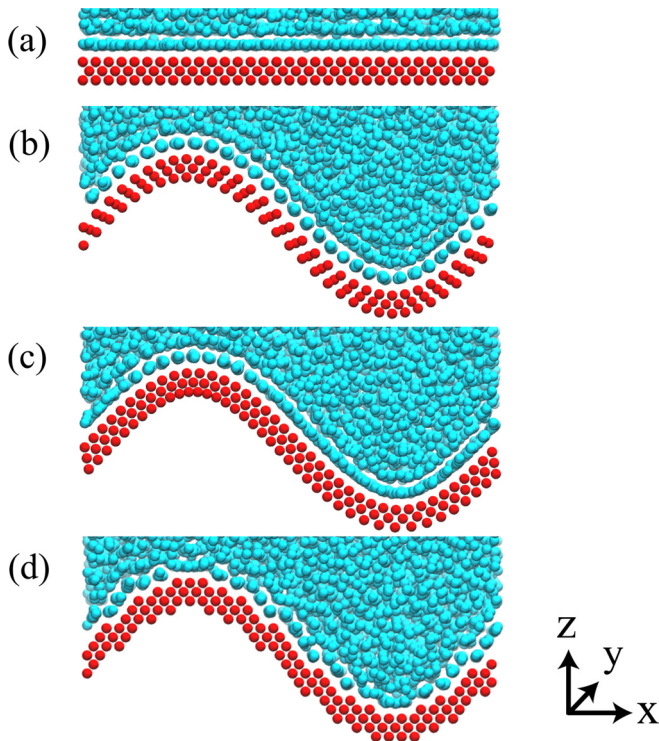
FIG. 2. Snapshots of the fluid atoms near (a) a flat surface and near three corrugated surfaces of different types: (b) type I, (c) type II, and (d) type III. The fluid and solid atoms are colored in cyan (light) and red (dark), respectively. The wall parameters are $a_0 = 0.75\sigma$, $\epsilon_{wf} = 1.8\epsilon$, and $\sigma_{wf} = 1\sigma$ and the corrugation amplitude A is around 4σ. The systems are at equilibrium.

respectively. With the bottom wall kept stationary, Couette-type shear flow is generated by moving the top wall along either the x or y direction at a speed $U_w = 1\sigma\tau^{-1}$, so the flow boundary conditions are measured separately for the two directions. As described below, the interactions between the fluid and top wall are chosen so that there is no slip.

Wall atoms are fixed rigidly to lattice sites.[1] If not stated elsewhere, each flat wall consists of three (001) layers of an fcc crystal with nearest-neighbor spacing a_0 [Figs. 1 and 2(a)]. The x axis is aligned with the [110] vector of the fcc lattice (nearest-neighbor direction). The nominal position of the wall surface is defined by the height of wall atoms in the layer closest to the fluid. The top wall is flat and the surface is placed at height $z = H$. If the bottom wall is flat, its surface is located at $z = 0\sigma$.

Three different methods are used to create sinusoidal bottom walls, resulting in three types of atomic scale structures, as depicted in Fig. 2.

(i) A type I wall [Fig. 2(b)] is constructed by displacing the solid atoms of a flat wall along the z direction by a distance $\Delta z(x) = A \sin(2\pi x/\lambda_x)$ [15]. The parameters A and λ_x denote the amplitude and wavelength of the corrugation, respectively. As shown in Fig. 2(b), the displacement deforms the lattice structure of the wall. The lateral spacing between the nearest-neighbor atoms along the surface layer increases with the absolute value of the local slope.

————

[1]Including thermal oscillations about lattice sites changes numerical values but not trends, including the relation between slip and in-plane order discussed in Sec. II B [7].

TABLE I. Parameters of the five groups of solid bottom walls presented in this paper, i.e., the lattice constant of the flat wall a_0, the interaction energy ϵ_{wf}, the interaction length σ_{wf}, and the intrinsic slip length $L_{s,0}$ at (001) and (111) surfaces along the [110] direction.

Index	a_0/σ	ϵ_{wf}/ϵ	σ_{wf}/σ	$L_{s,0}/\sigma$ (001)	(111)
A	1.20	0.4	1	0.56	1.54
B	1.20	1.8	1	−1.11	−0.29
C	1.20	0.00024	2.00	7.35	13.18
D	0.75	0.4	1	10.96	22.66
E	0.75	1.8	1	0.73	8.42

(ii) A type II wall [Fig. 2(c)] is also made by curving a flat wall along the x direction so that the atoms of the surface layer adjacent to the fluid follow the curve $z(x) = A\sin(2\pi x/\lambda_x)$, but the lateral spacing between neighbors is kept constant. The atomic arrangement along the y direction remains unchanged. Additional rows of atoms along the x direction are included in each layer, to ensure that the surface layer has a locally square structure with nearest-neighbor spacing a_0 as in the original flat surface [17,52]. The number of rows must be an integer and the period L_x is increased to 48.17σ to allow us to sample more amplitudes in the range of interest.

(iii) A type III wall [Fig. 2(d)] is carved out from an fcc crystal with the same atomic arrangement as the flat wall. All atoms above the sinusoidal wave $z(x) = A\sin(2\pi x/\lambda_x)$ are removed [60]. Special care is taken to choose the height of lattice planes so that the heights of surface steps are symmetric about the x-y plane ($z = 0$).

The type I and II surfaces are referred to as bent surfaces, while the type III surfaces are called stepped surfaces. At zero amplitude $A = 0\sigma$, the fcc (001) flat surface is recovered for all three types. If not stated elsewhere, $H = 30\sigma$, $L_x = L_y = 24.08\sigma$, and $\lambda_x = 24.08\sigma$. Varying λ_x by a factor of 2 produces similar trends in the effective slip length.

The lateral separation of the nearest-neighbor atoms in the surface layer is an important parameter of the wall, because it determines the characteristic length of the atomic scale roughness in the wall potential experienced by fluid atoms. It regulates not only the degree of local slip, but also how the slip varies in response to wall curvature [7,52]. In this study we investigate effective slip boundary conditions for both sparse ($a_0 = 1.2\sigma$) and close-packed ($a_0 = 0.75\sigma$) walls, where the lateral spacings at the original flat surfaces are respectively larger and smaller than the characteristic spacing of the fluid atoms. Our previous studies of curved surfaces showed that these wall spacings provide interesting limiting cases of high and low density [52]. The different sets of wall-fluid interaction parameters studied are listed in Table I. If not mentioned otherwise, $\sigma_{wf} = 1\sigma$. When ϵ_{wf} is decreased or σ_{wf} is increased, the wall-fluid coupling is weakened and slip is enhanced. The top wall is kept at $a_0 = 1.2\sigma$. No-slip boundary conditions are always enforced at top surfaces by using large values of ϵ_{wf}.

B. Fluid structure near the wall

In general, two types of structure are induced in a fluid in contact with a solid surface: density layering perpendicular to the surface and epitaxial ordering within the layers. Examples of the layering effect near flat walls are presented in Fig. 3 for the various wall parameters listed in Table I. The fluid density profiles oscillate near solid walls and gradually relax to the uniform bulk value far away from the walls. Several layers can be identified with peaks in the profiles that are separated by density minima [7,10,13,52,61–70]. The position and strength of the first peak are determined mainly by the wall-fluid interaction and the relative spacing of fluid atoms and the minima in the wall potential. However, the strength of the layering effect does not necessarily correlate with the degree of fluid slippage at the solid surface [7,11–13,15,71–75].
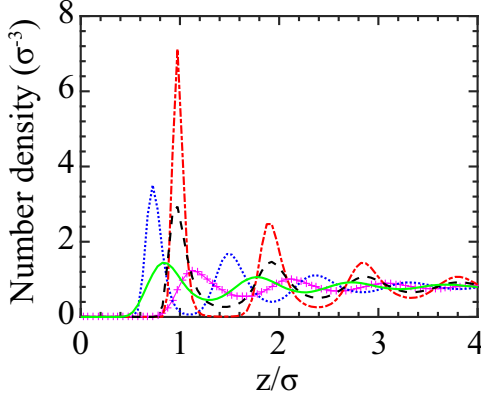
FIG. 3. Fluid density as a function of distance from the wall surface for flat surfaces with the parameters tabulated in Table I: A (solid green line), B (dotted blue line), C (solid magenta line with crosses), D (dashed black line), and E (dash-dotted red line). The hydrodynamic boundary condition is defined relative to the height of the first density peak $d_{1,0}$ for each case.

Previous studies have shown that the flow boundary condition for a simple fluid is instead correlated with the amount of epitaxial order within the first fluid layer induced by the atomic-scale roughness in the wall potential [7,11–13,15,52,71–75]. To describe the in-layer structure at a flat surface, the two-dimensional (2D) static structure factor $S_1(\vec{q})$ is calculated as a function of wave vector $\vec{q}$ for the first layer of fluid atoms:

$$S_1(\vec{q}) = S_1(q_x, q_y) = \left| \sum_j \exp[i(q_x x_j + q_y y_j)] \right|^2 \Big/ N_1, \qquad (3)$$

where x_j and y_j are the 2D coordinates of atom j and N_1 is the number of fluid atoms in the first layer. The allowed wave vectors are determined by the periods of the system in the x-y plane $\vec{q} = (2\pi h/L_x, 2\pi k/L_y)$, where h and k are integers. The periodic potential of the wall induces Bragg peaks at the corresponding reciprocal lattice vectors $\vec{G}_{m,n}$ of the wall. For the fcc (001) surface, $\vec{G}_{m,n} = (2\pi m/a_0, 2\pi n/a_0)$. More generally, if the nearest-neighbor spacings along x and y (denoted by a_x and a_y, respectively) are different from each other, $\vec{G}_{m,n} = (2\pi m/a_x, 2\pi n/a_y)$.

The structure factors for flat walls shown in Sec. III A are obtained in the equilibrium state. Structure factors are typically evaluated every 0.05τ and temporally averaged over up to 500τ.

C. Determining intrinsic and effective slip lengths

For a Newtonian fluid flow past an impenetrable solid surface, Navier's slip model assumes that the drag per unit area on the fluid from the solid surface is proportional to the relative velocity Δu_t of the two, which is also referred to as the slip velocity. This drag force is balanced by the viscous shear stress Π_{nt} of the fluid at the surface, where n represents the normal direction to the surface (pointed into the fluid) and t denotes the direction of the slip velocity that is tangential to the surface. The drag coefficient is typically written as μ/L_s,

$$\frac{\mu}{L_s} \Delta u_t = \Pi_{nt}, \qquad (4)$$

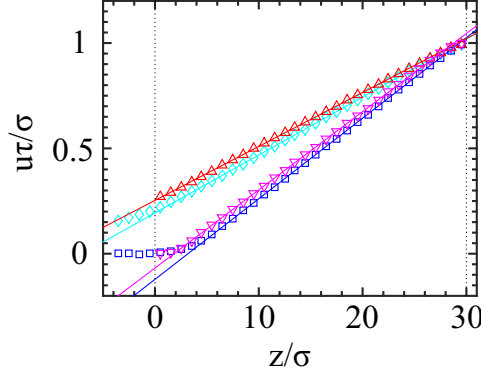where μ is the Newtonian viscosity and the intrinsic slip length L_s quantifies the degree of slip.

FIG. 4. Velocity profiles for four cases: flat surfaces at $a_0 = 1.20\sigma$ and $\epsilon_{wf} = 1.8\epsilon$ (magenta downward triangles) and $a_0 = 0.75\sigma$ and $\epsilon_{wf} = 0.4\epsilon$ (red upward triangles) and sinusoidal surfaces with $A = 4\sigma$, $a_0 = 0.75\sigma$ and $\epsilon_{wf} = 0.4\epsilon$ in the transverse (blue squares) and longitudinal (cyan diamonds) directions. Solid colored lines show fits to Eq. (7) and dotted vertical black lines show the positions $z = 0$ and H.

For a flat surface, the viscous stress is related to the strain rate by Newton's law

$$\Pi_{nt} = \mu \frac{\partial u_t}{\partial n}. \tag{5}$$

Combining Eqs. (4) and (5), one arrives at the conventional Navier slip boundary condition

$$\Delta u_t = L_s \frac{\partial u_t}{\partial n}. \tag{6}$$

Here the slip length L_s corresponds to the distance below the surface where the relative velocity of the fluid extrapolates to zero. For flow along a curved surface, an extra term associated with the surface curvature emerges naturally in the strain rate and thus Eq. (6) needs to be modified [21,76].

For planar Couette flow between two flat surfaces, the incompressible Newtonian Navier-Stokes equations reduce to $\mu \partial^2 u_x / \partial z^2 = \partial \Pi_{xz} / \partial z = 0$. Solving this equation, one arrives at a linear velocity profile

$$u_x = A_1 z + A_2. \tag{7}$$

The two constants A_1 and A_2 are determined by the boundary conditions at the wall-fluid interfaces.

Mean velocity profiles from two different flat surfaces are presented in Fig. 4 and manifest very different behaviors at the stationary bottom surface. For the close-packed surface with $a_0 = 0.75\sigma$ and $\epsilon_{wf} = 0.4\epsilon$, the remarkable velocity difference at the wall signifies a substantial slip. For the sparse surface with $a_0 = 1.20\sigma$ and $\epsilon_{wf} = 1.8\epsilon$, the fluid velocity vanishes inside the fluid, indicating that the fluid atoms in contact with the surface are locked to the wall [7]. This corresponds to a stick boundary condition. In the bulk region several atomic diameters away from wall, both of the profiles can be well fitted by the linear velocity profile [Eq. (7)].

Evaluating the slip length from the fitted linear velocity profile [Eq. (7)] requires a definition for the position of the hydrodynamic boundary. We choose the height of the density peak associated with the first fluid layer (Fig. 3) $d_{1,0}$ as the hydrodynamic boundary [52]. The intrinsic slip length at the bottom surface is then obtained from the fit coefficients as

$$L_{s,0} = d_{1,0} + A_2/A_1. \tag{8}$$

The subscript 0 denotes that $L_{s,0}$ is measured at the flat surface. Because of the fourfold symmetry of the fcc (001) surface, the slip boundary condition is equivalent along both x and y. In past studies of intrinsic slip boundary conditions, other locations have also been adopted for the hydrodynamic

boundary, e.g., the wall surface [11,77], the middle between the wall surface and the first fluid density peak [7,74,75,78], and half an atomic diameter from wall [12,79]. These common choices for the reference plane differ by less than the layer spacing, resulting in a corresponding small ambiguity in the intrinsic slip length determined by Eq. (8).

Figure 4 also illustrates two mean velocity profiles over a sinusoidal type I surface with $A = 4\sigma$. For transverse flow (along x), the mean velocity vanishes below a height of about 4σ, indicating that fluid is trapped in the region between the crests of the sinusoidal surface and moves with the solid. This corresponds to an effective stick boundary condition. For longitudinal (y-direction) flow, the resistance from the sinusoidal corrugation is weaker. The flow is noticeable below the tops of the crests and even below $z = 0\sigma$, corresponding to an effective slip boundary condition. In the bulk region a few atomic diameters above the top of the bottom surface, both of the two flow profiles are nicely fitted by the linear solution for flat surfaces, i.e., Eq. (7).

The effective slip lengths $L_{\text{eff},x}$ and $L_{\text{eff},y}$ are determined using Eq. (8) and fits to the linear regions of flow profiles. Consistent with the intrinsic boundary conditions for flat surfaces, the horizontal plane $z = d_{1,0}$ is defined as the effective hydrodynamic boundary. Therefore, $L_{\text{eff},x} = L_{\text{eff},y} = L_{s,0}$ at flat surfaces where the wave amplitude becomes zero.

In the limits of interest here, linear response and creeping flow, the effective flow boundary condition at an arbitrary direction relative to the sinusoid can be determined by combining the transverse and longitudinal results [1,18,80]. In general, the drag coefficient at the wall can be described as a tensor whose components depend on the orientation of the sinusoidal roughness and crystalline lattice and the symmetry of the lattice [7,52,81]. Choosing the x and y directions to be along twofold axes of the substrate lattice and transverse and longitudinal to the sinusoidal modulation ensures that the off-diagonal matrix elements of the drag tensor vanish in our geometry. The solutions for motion of the top wall in different directions can be obtained by a simple superposition of the results for the transverse and longitudinal components of the top wall velocity with the corresponding slip length. The anisotropy in slip length will cause the direction of flow to rotate towards the direction with the largest slip length as the distance to the bottom surface decreases. We confirmed that this superposition was valid for several of the cases considered below. Deviations like those seen for flat surfaces with varying slip length in Ref. [79] were only found when the velocity difference at the wall was high enough ($>0.05\sigma/\tau$) that the boundary condition became nonlinear [8] or the shear rate was high enough to cause shear thinning in the bulk.

In simulations, the velocity profiles are averaged within horizontal bins of thickness $\Delta z = 1\sigma$ for a time period of 500τ at steady state. The resulting flow profile is fit to Eq. (7) over the region more than 4σ from the top of the surfaces. We verified that changing this condition by $\pm\sigma$ does not produce any noticeable changes. The slip length is then obtained from the fitted coefficients and further averaged over 20 consecutive time intervals.

In this study the Reynolds number, given by $\text{Re} = \rho H U_w/\mu$, is always around or below 10 [8,15,82]. We checked that in this low-Re regime, increasing the height H of the top wall (doubling in the MD simulations or increasing by a factor up to 10 in the continuum simulations) does not affect the measured effective slip length.

D. Continuum simulations

To isolate the effects from the atomic wall structure, continuum simulations are also performed for the same fluid flows. The effective slip lengths are calculated from the steady-state solutions of the incompressible Newtonian Navier-Stokes (NS) equations

$$\rho\vec{u} \cdot \vec{\nabla}\vec{u} = -\vec{\nabla}p + \mu\nabla^2\vec{u}, \tag{9}$$

$$\vec{\nabla} \cdot \vec{u} = 0. \tag{10}$$

The stress-based slip boundary condition of Eq. (4) is applied at the wall. The equations are solved numerically using an adaptive finite-element mesh with the software COMSOL MULTIPHYSICS

5.1. The mesh cell size is smallest (edge $<0.5\sigma$) near the walls and largest (edge $\sim 1\sigma$) in the bulk. We verified that further mesh refinement changed the effective slip length by less than the errors in atomistic simulations ($\sim 0.1\sigma$). As for atomic simulations, the effective slip length is evaluated from linear fits to the flow profiles away from the wall and Eq. (8). The reference hydrodynamic plane is $z = 0$.

Flows along the x direction are described by the two-dimensional NS equations in the x-z plane [15–17]. A periodic boundary condition is imposed along the x direction with a period of λ_x. The top wall is at $z = H$, moving at a speed U_w along x with a no-slip boundary condition. The stationary substrate is given by $z(x) = A \sin(2\pi x/\lambda_x)$.

For the flows along the y direction, the NS equations are solved in the three-dimensional domain that is created by extruding the two-dimensional domain in the y direction. A periodic boundary condition is imposed along the y direction with a period of 5σ. The top wall is moving at the speed U_w along y.

Unless otherwise specified, the boundary condition applied to the bottom surface has a constant local intrinsic slip length determined from MD simulations for the corresponding flat wall. For the cases of stick boundary conditions ($L_{s,0} < 0$), the bottom surface is shifted upward to $z(x) = A \sin(2\pi x/\lambda_x) + |L_{s,0}|$ and a no-slip boundary condition is applied on the shifted surface. The continuum solutions then represent a numerical solution of the same system studied analytically in the models of the next section without assumptions like small surface slope used in these analytic models. We also present continuum solutions for spatially varying local slip lengths along the wall and show that they are needed to explain deviations between simulations and analytic models.

E. Analytical models

Panzer and co-workers [21,76] analytically investigated the influence of weak sinusoidal corrugations on the effective slip length in the regime of Stokes flow. The key control parameter is the normalized amplitude KA, where $K = 2\pi/\lambda_x$ is the wave number and KA equals the maximum slope of the sinusoidal surface. Assuming the local intrinsic boundary condition to be the same as at a flat surface, they derived an approximation for the transverse slip length $L_{\text{eff},x}$:

$$L_{\text{eff},x} = \frac{L_{s,0}\omega_\infty(KA) - KA^2\omega_0(KA)/(1 + 2KL_{s,0})}{1 + K^3 A^2 L_{s,0}}, \tag{11}$$

where

$$\omega_0(KA) = \frac{1 - (KA)^2/4 + 19(KA)^4/64}{1 + (KA)^2 - (KA)^4/2} \tag{12}$$

and

$$\omega_\infty(KA) = \frac{1 - 5(KA)^2/4 + 61(KA)^4/64}{1 + (KA)^2 - (KA)^4/2}, \tag{13}$$

up to terms of order $(KA)^6$.

In the same limit, Kamrin *et al.* [18] also derived second-order asymptotic solutions for the effective slip lengths along both the transverse and longitudinal directions. If a small constant slip length $L_{s,0}$ is applied along the surface, the approximate expressions are given by

$$L_{\text{eff},x} \simeq L_{s,0} - KA^2, \tag{14}$$

$$L_{\text{eff},y} \simeq L_{s,0} - \tfrac{1}{2}KA^2. \tag{15}$$

As the amplitude increases, $L_{\text{eff},x}$ decreases twice as fast as $L_{\text{eff},y}$. The quadratic decay in the transverse direction has also been derived in Refs. [83–85].
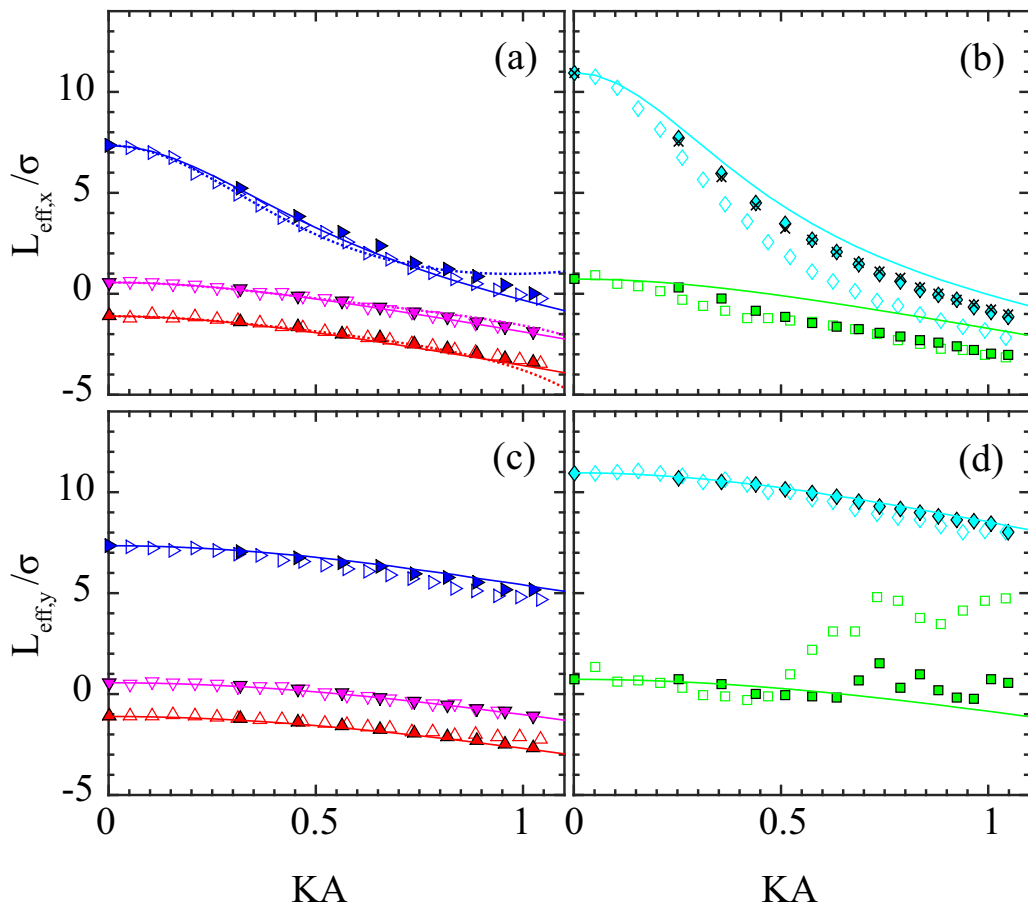
FIG. 5. (a) and (b) Effective transverse slip length $L_{\mathrm{eff},x}$ as a function of normalized roughness amplitude KA for types I (open symbols) and II (closed symbols) surfaces with (a) $a_0 = 1.2\sigma$ (triangles) and (b) $a_0 = 0.75\sigma$ (squares and diamonds). Results for the different wall parameters in Table I are indicated by symbol color and orientation: A (downward magenta triangles), B (upward red triangles), C (right-pointing blue triangles), D (cyan diamonds), and E (green squares). The dotted colored lines in (a) show the analytical prediction of Eq. (11). The solid colored lines represent the results from continuum simulations with the same local boundary condition as for the corresponding flat surface. The black crosses in (b) show the results from the continuum simulations with a density-corrected locally varying slip length. (c) and (d) Similar results for the longitudinal slip length $L_{\mathrm{eff},y}$ with (c) $a_0 = 1.2\sigma$ and (d) $a_0 = 0.75\sigma$. Statistical uncertainties in L_{eff} are about 0.1σ. Fluctuations in (d) reflect rapid changes in the structure of the first fluid layer.

III. RESULTS AND DISCUSSION

A. Bent surfaces

Figure 5 shows the variation with normalized roughness amplitude KA of the effective slip length for flow over bent surfaces in the transverse (x) and longitudinal (y) directions. Some general trends are seen for all cases. For flows transverse to the sinusoidal corrugations, increasing the amplitude significantly reduces $L_{\mathrm{eff},x}$. As $L_{s,0}$ increases, $L_{\mathrm{eff},x}$ drops more rapidly with increasing KA. For KA near unity, $L_{\mathrm{eff},x}$ tends to decrease linearly at a similar rate for all cases, which is consistent with previous continuum studies (both numerical and

analytical) [26,27,83,84,86,87].[2] The slip length in the longitudinal direction $L_{\mathrm{eff},y}$ also decreases monotonically for most cases, but more slowly than $L_{\mathrm{eff},x}$.

Despite these common general trends there are important differences in the behavior of dense and sparse walls. Results for sparse walls are relatively independent of wall type (I or II) and agree with continuum theory with a constant local slip length. In contrast, there are strong variations for dense walls that can only be understood by introducing a slip length that varies with the local curvature.

For the sparse surfaces ($a_0 = 1.20\sigma$), the three groups of LJ interaction parameters (Table I) yield three typical but very different intrinsic boundary conditions at flat surfaces. Slip is pronounced for $\epsilon_{wf} = 0.00024\epsilon$ and $\sigma_{wf} = 2\sigma$, where $L_{s,0} = 7.33\sigma$. For a stronger wall-fluid LJ interaction $\epsilon_{wf} = 0.4\epsilon$, $L_{s,0}$ drops to 0.56σ. The fitted velocity profile goes to zero in the region between the wall surface and the first fluid layer, indicating that there is little slip. When the interaction strength ϵ_{wf} is increased to 1.8ϵ, the first layer of fluid atoms becomes crystallized and locks into the wall potential minima. The locked first layer then further traps fluid atoms in the second layer through the fluid LJ interactions [7]. As a result, a negative slip length $L_{s,0} = -1.11\sigma$ is generated, corresponding to a stick boundary condition (also demonstrated in Fig. 4).

Adding atomic roughness to these sparse surfaces produces very similar decreases in the slip length for type I and II surfaces. For both transverse and longitudinal flows, these changes are nicely reproduced by numerical NS solutions that assume that the local slip length remains equal to that on a flat surface. Moreover, the simpler analytical models described in Sec. II E capture the trends in L_s. Indeed, the prediction of Panzer and co-workers [21,76] agrees with all simulations for $KA \lesssim 0.5$ and for almost the entire range of data for $\epsilon_{wf} = 0.4\epsilon$. Although not shown, the Kamrin et al. predictions agree with the results at $\epsilon_{wf} = 0.4\epsilon$ and 1.8ϵ up to $KA \sim 0.4$, for both MD and continuum simulations.

In contrast, the results for close-packed surfaces ($a_0 = 0.75\sigma$) are different for walls of types I and II and neither is consistent with continuum solutions with a constant local slip boundary condition. For $\epsilon_{wf} = 0.4\epsilon$ (blue diamonds), a large slip length $L_{s,0} = 10.96\sigma$ is measured for the flat surface. With increasing KA, type II surfaces have systematically larger $L_{\mathrm{eff},x}$ than type I. The numerical NS solutions yield even higher $L_{\mathrm{eff},x}$, particularly at large KA. Priezjev et al. [15] found a similar discrepancy in the same regime of high surface density and weak wall-fluid interactions.

Flat surfaces with $\epsilon_{wf} = 1.8\epsilon$ have a nearly no-slip boundary condition ($L_{s,0} \sim 0.7\sigma$) that is very similar to that for sparse surfaces with $\epsilon_{wf} = 0.4\epsilon$. Thus the continuum NS solutions for rough surfaces in Fig. 5 are nearly the same. However, roughness causes a much more rapid decrease in transverse slip length for dense surfaces. By $KA = 1$, both type I and II dense surfaces have very negative values of $L_{\mathrm{eff},x}$ that are close to the results for sparse surfaces with $\epsilon_{wf} = 1.8\epsilon$. The deviations in longitudinal slip are even more dramatic: $L_{\mathrm{eff},y}$ first drops rapidly and then rises and oscillates. Note that for type I surfaces $L_{\mathrm{eff},y}$ reaches up to $\sim 5\sigma$, which exceeds the amplitude of the corrugation.

The results for dense surfaces illustrate the kind of behavior that can occur whenever the curvature on rough surfaces changes the local slip boundary condition. The results for cylindrical surfaces in Ref. [52] explain the nature of the changes and why they are stronger for sparse surfaces than dense surfaces in Fig. 5. As noted in Sec. II B, the viscous coupling between fluid and solid is strongest when the wall potential produces strong density modulations in the first fluid layer. The fluid modulations are largest when the spacing between fluid atoms is comparable to the spacing between minima in the potential from wall atoms. Any mismatch produces a more rapid drop in coupling for dense surfaces than sparse surfaces. The reason is that fluid atoms can fit more easily between atoms on sparse walls, so the magnitude of the corrugation in wall potential is larger [52].

---

[2]In this limit, a weak vortex may form in the valley if the local slip is small [16,88], but the emergence of the vortex has little impact on the pattern of behavior of the effective slip length with varying KA in the low-Reynolds-number limit studied here [88].
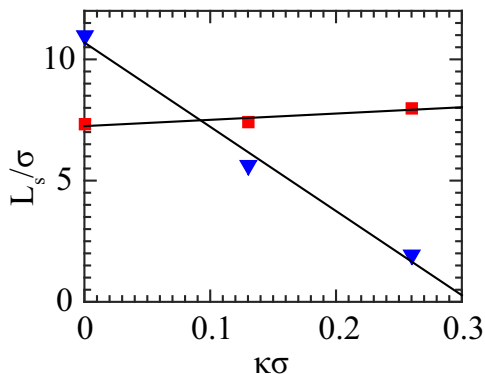
FIG. 6. Results of cylindrical-geometry MD simulations for the behavior of the intrinsic slip length L_s with increasing curvature κ from 0 to $0.26/\sigma$. Results for two sets of wall parameters in Table I are indicated by symbol type: C (red squares) and D (blue triangles). The former data are reported in the Supplemental Material of Ref. [52], while the latter were obtained in the same way using simulations of flow between concentric cylinders of constant curvature. The relation between L_s and κ is approximated by a linear fit, which is shown by the solid black lines.

For type II surfaces the spacing between wall atoms is fixed, but the spacing between potential minima changes with curvature because fluid atoms are at a different radius. For positive curvature the separation increases, while for negative curvature the separation decreases. These changes are visible in the snapshots shown in Figs. 2(b) and 2(c). The spacing between fluid atoms is larger near crests and smaller near troughs. Figure 6 shows the resulting variation in L_s with curvature for the sparse and dense surfaces with the largest slip lengths in Fig. 5. The dense results are from Ref. [52] and the sparse results were obtained in the same way using simulations of flow between concentric cylinders of constant curvature. The largest curvature $0.26\sigma^{-1}$ is close to the curvature at the crest of sinusoidal surfaces with $KA \sim 1$. Note that L_s changes by an order of magnitude for the dense walls, but is relatively constant for sparse walls.

To show that these curvature effects can quantitatively account for changes in transverse slip over type II surfaces we repeated the continuum NS calculations with varying local slip lengths. In all regions of positive curvature we used the linear fit to data shown in Fig. 6. In convex regions of negative curvature we used the slip length for flat surfaces. While local slip is expected to be enhanced in these regions [52], flow is already strongly suppressed and changes in L_s have little effect. Moreover, calculation of L_s for large negative curvatures is impractical since it would involve Couette flow between two cylinders where the outer has a radius of only three atoms.

Solutions of the NS continuum equations for sparse surfaces with curvature corrected local slip lengths were nearly identical to those for a fixed length and are not shown in Fig. 5(a). Variations in local slip do affect the continuum solution for dense walls and the crosses in Fig. 5(b) track the atomistic results for type II walls. Slip is even smaller for type I walls because the atomic spacing in the transverse direction grows with the local slope. This further reduces the local slip length and thus the average effective slip length of the surface. Priezjev *et al.* also noted that this increase in spacing reduced the slip length and incorporated it in continuum simulations with a modified slip boundary condition that was uniform rather than a function of local slope and curvature [15].

Curvature does not change the effective spacing between wall atoms along the longitudinal y direction. For the case considered here, the nearest-neighbor spacing and the reciprocal lattice vector $\vec{G}$ characterizing the density modulations are both along y. As a result, there is little change in the local L_s for longitudinal flows at small KA. This explains why type I and II walls have similar effective slip lengths that are both consistent with the NS solutions for constant local slip. If the lattice is rotated $45°$, the reciprocal lattice vectors have components along both transverse and

longitudinal directions. Reference [52] found that curvature then affected longitudinal flow more than transverse flow. We do not present results for this case because the changes in local slip length are in between the ones shown in Fig. 5.

Other researchers have considered the case of smooth surfaces with stripes of low and high slippage. Type I surfaces will have similar oscillations in local slip but with several important differences. As just noted, the changes in spacing only cause alternations in slip for flow along the transverse direction. In addition, these variations do not depend on the sign of the slope and so have a different period than the variations in slope. The combination of two effects with different periods makes it difficult to make a direct comparison of our results to these previous studies.

For large KA the longitudinal slip length for strongly interacting sparse walls [Fig. 5(d)] shows a sudden transition to new behavior. This reflects a transition in the structure of the first layer due to the strong change in local geometry produced by roughness. The strong change in the degree of epitaxial order is visible in Fig. 6. The large wall-fluid interaction strongly attracts fluid atoms to the surface, leading to a pronounced layering (Fig. 3). However, little lateral order can be seen within the first layer above the flat surface [Fig. 2(a)]. This is because the small spacing of the wall potential minima makes it difficult for the fluid atoms to lock into epitaxial order [7]. The positive curvature near crests in Figs. 2(b) and 2(c) leads to a larger spacing between minima in the potential from wall atoms and atoms in the first fluid layer align into lines going into the page. For type I surfaces the spacing is also increased on sloped regions and there is a corresponding increase in alignment that is not seen on type II surfaces.

The in-plane structure factor provides a more comprehensive and quantitative description of the changes in lateral order, but it can only be calculated for a large area with constant wall structure. To mimic the structure at the crest of the sinusoidal surface profile we create a flat surface with a rectangular structure. In one direction the nearest-neighbor spacing is the constant longitudinal spacing $a_0 = 0.75\sigma$. The spacing in the other direction is increased to the value 0.93σ, near a crest with $KA = 0.75$. Similar results were obtained for cylindrical surfaces with the same spacings, so we expect the results to be representative of the local structure at wave crests.

Figure 7(a) shows the structure factor S_1 for the reference flat surface with a square lattice structure. Normalizing by N_1 gives a quantity that reaches unity for a perfect crystal at zero temperature. Only positive q_x and q_y are shown since the surface is symmetric about both axes. Two Bragg peaks are found at the shortest reciprocal vectors $\vec{G}_{1,0}$ and $\vec{G}_{0,1}$. The heights are small (0.03) because the minima are too closely spaced for fluid atoms to lock into. The two higher peaks with magnitudes around 0.25 are associated with high-order commensurate phases that are a better match with the fluid spacing [7]. The first fluid layer has an intermediate viscous coupling to the wall, corresponding to a slip length close to zero.

Figure 7(b) presents $S_1(\vec{q}\,)/N_1$ on a surface with wall atom spacing increased to 0.93σ along the x direction, reducing the symmetry from fourfold to twofold. Because this increased spacing is close to the mean spacing between fluid atoms, there is strong epitaxial order reflected in large peaks at the first and second Bragg vectors. Indeed, the height (0.82) of the first peak at $\vec{G}_{1,0}$ is above the value for bulk solids at the liquid-solid transition ($\sim$0.6). In contrast, there are no visible peaks along q_y at $\vec{G}_{0,1}$ because the lattice spacing remains small. Instead there is a peak at a high-order commensurate structure with 16 fluid atoms per 21 wall atoms. This highly anisotropic structure leads to anisotropic slip boundary conditions. The first fluid layer is locked to the lattice in the x direction and even the second layer experiences a strong viscous drag. In contrast, the first layer slides even more easily in the y direction than for the square lattice. The slip length increases by an order of magnitude to about 5σ.

These changes in fluid structure explain the results for strongly interacting dense surfaces in Figs. 5(b) and 5(d). The stretched spacing at the crest gives a strong reduction in local transverse slip length. The strong pinning of atoms at the crest inhibits sliding of the entire first layer. This lowers $L_{\text{eff},x}$ relative to the continuum NS solution for $KA > 0.5$ and $L_{\text{eff},x}$ approaches the solution for strongly interacting sparse surfaces that have a local stick boundary condition. The opposite effect
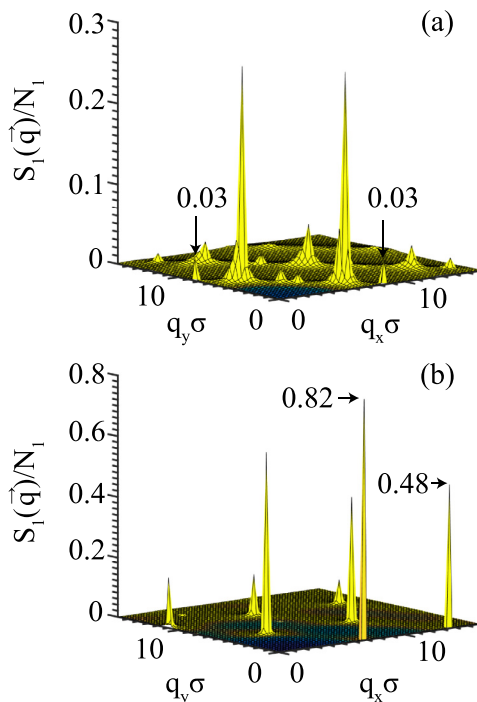
FIG. 7. In-plane order as characterized by the normalized structure factor $S_1(\vec{q})/N_1$ on flat surfaces where $a_0 = 0.75\sigma$ and $\epsilon_{wf} = 1.8\epsilon$. Results for (a) the fcc (001) surface and (b) a surface that is uniformly stretched along x, so the lateral spacing along x is increased from 0.75σ to 0.93σ.

occurs in the longitudinal direction. The sharp increase in the local longitudinal slip length at the crest leads to a rapid rise in Fig. 5(d). The effect is largest for the type I surfaces where the stretched spacing extends beyond the crest into regions where the surface slope is high. The high-order commensurate phases are sensitive to the exact degree of stretching, leading to fluctuations in the magnitude of the increase as KA rises.

B. Stepped surfaces

Figure 8 presents the effective slip length on the stepped surfaces as a function of KA, for the x and y directions. The stepped surfaces are generated using sine waves with A increasing from 0 to 4σ in increments of 0.2σ. All atoms on lattice sites below the sine wave are removed. Because atoms lie at discrete positions, the total height variation has only a few discrete values and different amplitude sine waves can generate the same surface. In Fig. 8 we use the smallest A that produces a given atomic configuration and each point in Fig. 8 corresponds to a different configuration. Results for the type I bent surfaces are also presented for reference.

Surface steps have the most profound affect on flow in the transverse direction. The step edges trap fluid atoms in the adjacent layer, generating an additional drag force that dramatically reduces the local slip. As a result, $L_{\mathrm{eff},x}$ drops significantly for slippery surfaces with $L_{s,0} \gg \sigma$ [right-pointing triangles in Fig. 8(a) and diamonds in Fig. 8(b)]. This effect is less noticeable for cases with nearly no slip or stick boundary conditions since the drag is already high when the surface is flat [downward and upward triangles in Fig. 8(a) and squares in Fig. 8(b)].

For slippery surfaces, $L_{\mathrm{eff},x}$ decreases in a stepwise manner. Each step corresponds to an increase in the total height change along the surface. To facilitate comparison with bent surfaces, we define an
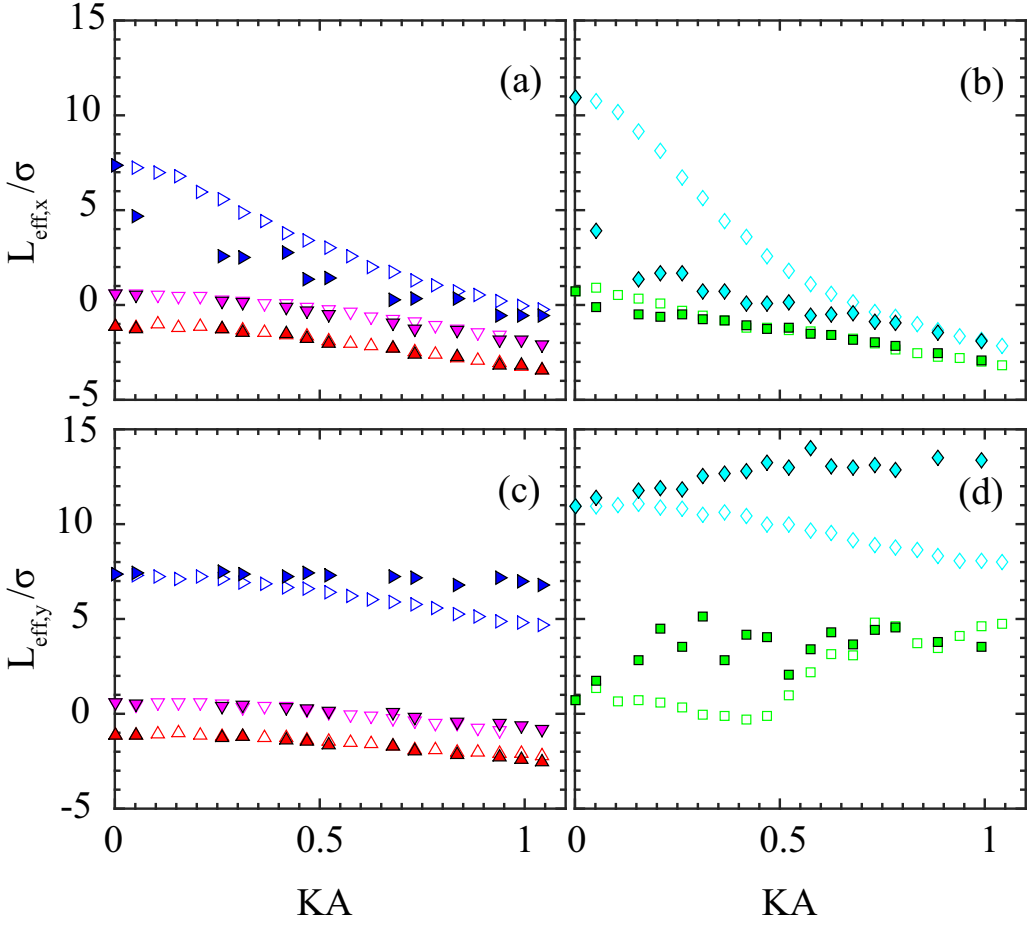
FIG. 8. (a) and (b) Effective transverse slip length $L_{\mathrm{eff},x}$ over the bent type I (open symbols) and stepped type III (closed symbols) surfaces with (a) $a_0 = 1.2\sigma$ and (b) 0.75σ as a function of the normalized amplitude KA. The various wall parameters from Table I are indicated by symbol color and orientation: A (downward magenta triangles), B (upward red triangles), C (right-pointing blue triangles), D (cyan diamonds), and E (green squares). (c) and (d) Effective longitudinal slip length $L_{\mathrm{eff},y}$ for the surfaces in (a) and (b), respectively. Statistical uncertainties in L_{eff} are about 0.1σ. Fluctuations in (d) reflect rapid changes in the structure of the first fluid layer.

amplitude $A_{\mathrm{real}} = \Delta h/2$, where Δh is the height difference between the highest and lowest surface wall atoms. For the (001) surfaces considered here, $\Delta h = ma_0/\sqrt{2}$, where m is an integer and $a_0/\sqrt{2}$ is the spacing between lattice planes perpendicular to the surface. For $KA_{\mathrm{real}} < 1$, the surface height changes in steps of $a_0/\sqrt{2}$, and if $\Delta h = ma_0/\sqrt{2}$ there are m steps up and m steps down per period. The discrete changes in $L_{\mathrm{eff},x}$ in Figs. 8(a) and 8(b) correspond to changes in m, indicating that drag scales with the density of step edges.

Figure 9 shows a quantitative test of the contribution of step edges. For large slip lengths, the effective damping is inversely proportional to L_{eff}. Flat regions provide a background damping proportional to $\sigma/L_{s,0}$. The number of atomic steps per unit length is $2m/\lambda_x \propto KA_{\mathrm{real}}$. Figure 9(a) shows that the drag rises linearly with KA_{real} with results for different λ_x collapsing onto a universal curve. Similar results were found for (111) surfaces and other wall interactions. Note that the slopes are different for sparse and dense surfaces, indicating that each step on a sparse surface produces
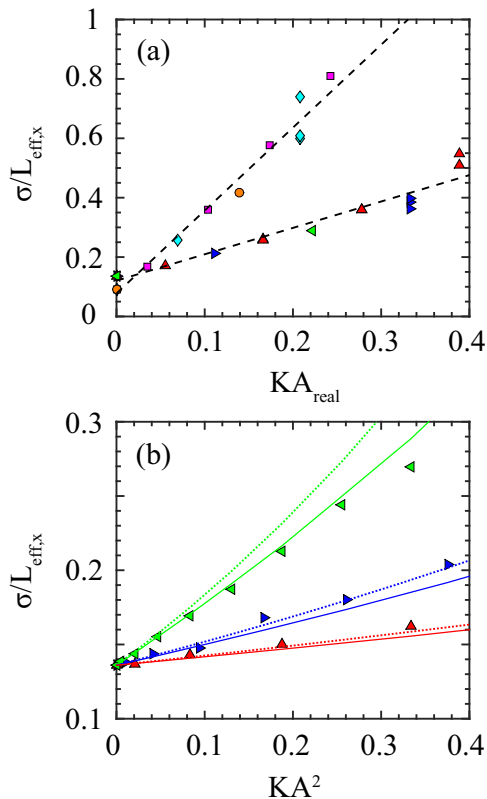
FIG. 9. (a) Plot of $\sigma/L_{\mathrm{eff},x}$ as a function of KA_{real}, where A_{real} is the total roughness amplitude of stepped surfaces, for three wavelengths: $\lambda_x = 12.04\sigma$ (left-pointing green triangles and orange circles), 24.08σ (right-pointing blue triangles and cyan diamonds), and 48.17σ (upward red triangles and magenta squares). Symbol type indicates the wall parameters from Table I: C (triangles) and D (squares, diamonds, and circles). Black dashed lines are linear fits to the data for each set of wall parameters. (b) Plot of $\sigma/L_{\mathrm{eff},x}$ as a function of KA^2 for the sparse surface with set D wall parameters from Table I. The dotted colored lines show the analytical prediction of Eq. (11). The solid colored lines represent the results from continuum simulations with the same local boundary condition as for the corresponding flat surface.

less drag. We find that a number of factors may affect the drag from step edges. For Fig. 9(a), the main factor is that the larger $\sigma_{wf} = 2\sigma$ for sparse surfaces rounds out the potential from the step edge. For the same interaction parameters, lowering the ratio of step height to the height of the first fluid layer reduces the drag. In all cases studied, the drag scaled linearly with KA_{real}.

This linear scaling is inconsistent with the analytical results for continuous surfaces [Eq. (11)]. There the damping rises as KA^2 as roughness rises from zero. Figure 9(b) verifies this scaling for type I surfaces. Note that the detailed analytical theory [Eq. (11)] provides a good quantitative fit at small KA^2. The simpler approximation [Eq. (14)] predicts the correct linear dependence on KA^2, but not the change in slope with wavelength. The change in slope comes from terms in $KL_{s,0}$ in Eq. (11). Our simulation results verify the analytic form of these terms for bent surfaces. Deviations from the asymptotic behavior become evident at smaller KA^2 as the wavelength decreases because curvature begins to affect the local slip boundary condition.

Step edges have the opposite effect on longitudinal flow, tending to increase the slip length compared to bent surfaces. As shown in Figs. 8(c) and 8(d), the effect is particularly pronounced for surfaces where the damping on flat surfaces is low, i.e., $L_{s,0}$ is high. For the two most slippery
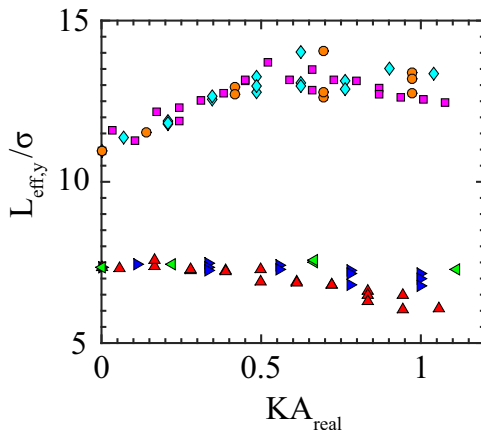
FIG. 10. Effective longitudinal slip length $\sigma/L_{\text{eff},y}$ as a function of KA_{real} for three wavelengths: $\lambda_x = 12.04\sigma$ (left-pointing green triangles and orange circles), 24.08σ (right-pointing blue triangles and cyan diamonds), and 48.17σ (upward red triangles and magenta squares). Symbol type indicates the wall parameters from Table I: C (triangles) and D (squares, diamonds, and circles). Black dashed lines are linear fits to the data for each set of wall parameters.

surfaces the slip length can be enhanced by $\sim$50% at large KA. For the less slippery surfaces the slip length may increase from nearly zero to 5σ.

We found that step edges lowered the drag for longitudinal flow by changing the structure of the first fluid layer. Fluid atoms near step edges are ordered into parallel lines. This alignment propagates away from the edges, increasing density modulations in the transverse direction. In contrast, there is less order in the longitudinal direction. As noted above and in earlier work [7,52,89–91], the slip length scales inversely with the degree of epitaxial order at Bragg vectors along the flow direction. Measurements of $S_1(\vec{G}_{0,1})/N_1$ show that the wall-induced Bragg peak along the longitudinal direction is decreased by step edges. For example, for $e_{wf} = 0.4\sigma$ and $a_0 = 0.75\sigma$ (diamonds) the peak in the first fluid layer above the lowest step may be reduced by 40%. There is a corresponding large increase in slip length for stepped surfaces relatively to bent surfaces. For the less slippery sparse case (squares) the reduction in Bragg peak is more dramatic because step edges hasten the transition to the ordered structure shown in Fig. 7. Rapid variations in order with KA lead to rapid fluctuations in L_s, as seen in Fig. 5(d).

Figure 10 shows the longitudinal slip length for different wavelengths in systems with large intrinsic slip lengths $L_{s,0}$. As for transverse slip, results for all wavelengths collapse when plotted against KA_{real}, indicating that slip only depends on the number of edges per unit length. Each edge induces local transverse order and lowers longitudinal order, leading to a rise in $L_{\text{eff},y}$. Continuum theory predicts a very different scaling, with changes in slip varying as KA^2.

A new effect was observed at very large KA_{real}. Adjacent step edges form close-packed (111) planes. The intrinsic slip length on these planes is larger, as noted previously by Soong *et al.* [81]. This decrease reflects the smaller spacing between minima in the wall potential, which reduces the degree of epitaxial locking in the adjacent fluid layer [7,52,91].

IV. CONCLUSION

We have used molecular dynamics simulations to study the effective slip boundary condition for simple fluid flow over rough surfaces in the Wenzel state and limit of linear response. The wall roughness was modeled by a one-dimensional sine wave with wavelength much larger than the atomic diameter. The uncovered atomic effects may also apply to other types of rough surfaces, e.g., surfaces with small bumps [19]. The behavior of the effective slip length was examined by increasing the

normalized corrugation amplitude up to $KA \sim 1$, for both the transverse and longitudinal directions. Results for other directions can be obtained by combining these results using the tensoral nature of the drag between solid and fluid (Sec. II C) [1,18,80]. Different atomic configurations were investigated for strong and weak wall-fluid interactions and high and low wall densities.

Increasing the roughness amplitude always reduces the transverse slip length $L_{\mathrm{eff},x}$. In most cases, it also decreases the longitudinal slip length $L_{\mathrm{eff},y}$, but at a slower rate. However, in some cases $L_{\mathrm{eff},y}$ shows a remarkable increase above $L_{s,0}$ that is in stark contrast to continuum predictions. The resulting effective boundary condition is highly anisotropic.

The results for bent surfaces can be understood by supplementing continuum theory with an appropriate local boundary condition that depends on curvature and atomic spacing [15,52]. For sparse bent surfaces, curvature has little effect on the local slip boundary condition (Fig. 6). For these surfaces the numerical solutions of the Navier-Stokes conditions with the flat surface slip length $L_{s,0}$ provide a good description of the slip length at roughness amplitudes up to $KA = 1$. Simpler analytic approximations [Eq. (11)] remain accurate to $KA \sim 0.5$. The largest deviations are associated with changes in the spacing between surface atoms, which are present on type I surfaces and eliminated for type II surfaces.

Larger deviations from simple continuum theory are seen for dense bent surfaces. Previous work [52] and Fig. 6 show that the local slip length on these surfaces is strongly dependent on curvature. For the chosen atomic orientation the curvature dependence is strong for transverse flow and negligible for longitudinal flow. As a result, the effect on the total transverse slip length is larger in Fig. 5. Including the curvature-dependent slip length in solutions of the Navier-Stokes equation captures the variation of the total effective slip length for type II surfaces. For type I surfaces the increase in atomic spacing on sloped surfaces produces an even greater suppression of slip.

The most dramatic deviation from continuum theory for bent surfaces occurs for flow over strongly interacting type I surfaces. The increase in atomic spacing along the transverse direction leads to anisotropic reconstruction of the first fluid layer. The layer becomes more strongly locked in the transverse direction, leading to a lower transverse slip length. However, the order in the longitudinal direction decreases and there is a dramatic change from a stick boundary condition to a longitudinal slip length that is larger than the amplitude of the roughness.

Steps lead to a qualitative change in the scaling of slip with surface roughness. There is a new contribution to drag from step edges that is independent of the slip length on flat surfaces. Results for transverse flow at different wavelengths collapse when plotted against KA_{real}, which is proportional to the density of step edges. This confirms that each edge adds an independent contribution to slip reduction. In contrast, results for bent surfaces show the scaling predicted by continuum theory, with drag rising as KA^2.

While steps suppress transverse slip, they enhance longitudinal slip. This was found to reflect alignment of fluid at step edges that suppressed longitudinal order. This contribution to changes in slip length also collapses when plotted against the step density at low KA_{real}. Different crystalline facets with higher or lower $L_{s,0}$ may form on rougher surfaces and lead to more complex behavior. For example, (111) facets (Fig. 2) with a larger slip length formed on the roughest surfaces in Fig. 8. Changes in the direction of the step edge along the surface will mix the effect of transverse and longitudinal regions. Since the drag enhancement due to transverse regions is larger, the net effect is likely to be a reduction in slip length.

We hope that the behavior revealed here will cast light on the behavior of realistic surfaces and facilitate the design of surfaces for various applications, e.g., drag reduction, flow control, and water harvesting. Real surfaces are likely to have more complex roughness with a range of wavelengths and orientations. Our results suggest that the resulting changes in slip will depend strongly on the atomic structure. The bent surfaces described here may represent various long-wavelength corrugations or rough amorphous surfaces. Such surfaces could be modeled with continuum theory using an appropriate local boundary condition determined for small surfaces of fixed curvature. The stepped surfaces studied here may be more representative of crystals. The results suggest that slip over such surfaces can be expressed in terms of the local slip length of faceted regions and an additional drag

due to the density of step edges transverse to flow. This additional term is very sensitive to details of the atomic structure of the fluid and step edge, as well as the distribution of step edge angles.

---

[1] H. A. Stone, A. D. Stroock, and A. Ajdari, Engineering flows in small devices: Microfluidics toward a laboratory-on-a-chip, Annu. Rev. Fluid Mech. **36**, 381 (2004).

[2] E. Lauga, M. P. Brenner, and H. A. Stone, Microfluidics: The no-sip boundary condition, in *Springer Handbook of Experimental Fluid Mechanics*, edited by C. Tropea, A. Yarin, and F. F. Foss (Springer, New York, 2007), p. 1219.

[3] C. Neto, D. R. Evans, E. Bonaccurso, H.-J. Butt, and V. S. J. Craig, Boundary slip in Newtonian liquids: A review of experimental studies, Rep. Prog. Phys. **68**, 2859 (2005).

[4] L. Bocquet and J.-L. Barrat, Flow boundary conditions from nano-to micro-scales, Soft Matter **3**, 685 (2007).

[5] C. Denniston and M. O. Robbins, General continuum boundary conditions for miscible binary fluids from molecular dynamics simulations, J. Chem. Phys. **125**, 214102 (2006).

[6] C. L. M. H. Navier, Mémoire sur les lois du mouvement des fluides, Mémoires de l'Académie Royale des Sciences de l'Institut de France **6**, 389 (1823).

[7] P. A. Thompson and M. O. Robbins, Shear flow near solids: Epitaxial order and flow boundary conditions, Phys. Rev. A **41**, 6830 (1990).

[8] P. A. Thompson and S. M. Troian, A general boundary condition for liquid flow at solid surfaces, Nature (London) **389**, 360 (1997).

[9] M. Cieplak, J. Koplik, and J. R. Banavar, Boundary Conditions at a Fluid-Solid Interface, Phys. Rev. Lett. **86**, 803 (2001).

[10] T.-M. Galea and P. Attard, Molecular dynamics study of the effect of atomic roughness on the slip length at the fluid-solid boundary during shear flow, Langmuir **20**, 3477 (2004).

[11] N. V. Priezjev, Effect of surface roughness on rate-dependent slip in simple fluids, J. Chem. Phys. **127**, 144708 (2007).

[12] N. Priezjev, Rate-dependent slip boundary conditions for simple fluids, Phys. Rev. E **75**, 051605 (2007).

[13] J.-L. Barrat and L. Bocquet, Influence of wetting properties on hydrodynamic boundary conditions at a fluid/solid interface, Faraday Discuss. **112**, 119 (1999).

[14] A. E. Kobryn and A. Kovalenko, Molecular theory of hydrodynamic boundary conditions in nanofluidics, J. Chem. Phys. **129**, 134701 (2008).

[15] N. V. Priezjev and S. M. Troian, Influence of periodic wall roughness on the slip behavior at liquid/solid interfaces: Molecular-scale simulations versus continuum predictions, J. Fluid Mech. **554**, 25 (2006).

[16] A. Niavarani and N. V. Priezjev, The effective slip length and vortex formation in laminar flow over a rough surface, Phys. Fluids **21**, 052105 (2009).

[17] A. Niavarani and N. Priezjev, Modeling the combined effect of surface roughness and shear rate on slip flow of simple fluids, Phys. Rev. E **81**, 011606 (2010).

[18] K. Kamrin, M. Z. Bazant, and H. A. Stone, Effective slip boundary conditions for arbitrary periodic surfaces: The surface mobility tensor, J. Fluid Mech. **658**, 409 (2010).

[19] K. Sarkar and A. Prosperetti, Effective boundary conditions for Stokes flow over a rough surface, J. Fluid Mech. **316**, 223 (1996).

[20] M. Sbragaglia and A. Prosperetti, Effective velocity boundary condition at a mixed slip surface, J. Fluid Mech. **578**, 435 (2007).

[21] P. Panzer, M. Liu, and D. Einzel, The effects of boundary curvature on hydrodynamic fluid flow: Calculation of slip lengths, Int. J. Mod. Phys. B **06**, 3251 (1992).

[22] S. Granick, Y. Zhu, and H. Lee, Slippery questions about complex fluids flowing past solids, Nat. Mater. **2**, 221 (2003).

[23] Y. Zhu and S. Granick, Limits of the Hydrodynamic No-Slip Boundary Condition, Phys. Rev. Lett. **88**, 106102 (2002).

[24] R. Pit, H. Hervet, and L. Léger, Direct Experimental Evidence of Slip in Hexadecane: Solid Interfaces, Phys. Rev. Lett. **85**, 980 (2000).

[25] C. Kunert, J. Harting, and O. I. Vinogradova, Random-Roughness Hydrodynamic Boundary Conditions, Phys. Rev. Lett. **105**, 016001 (2010).

[26] C. Kunert and J. Harting, Roughness Induced Boundary Slip in Microchannel Flows, Phys. Rev. Lett. **99**, 176001 (2007).

[27] J. Harting, C. Kunert, and J. Hyväluoma, Lattice Boltzmann simulations in microfluidics: Probing the no-slip boundary condition in hydrophobic, rough, and surface nanobubble laden microchannels, Microfluid. Nanofluid. **8**, 1 (2010).

[28] G. McHale and M. I. Newton, Surface roughness and interfacial slip boundary condition for quartz crystal microbalances, J. Appl. Phys. **95**, 373 (2004).

[29] O. I. Vinogradova, N. F. Bunkin, N. V. Churaev, O. A. Kiseleva, A. V. Lobeyev, and B. W. Ninham, Submicrocavity structure of water between hydrophobic and hydrophilic walls as revealed by optical cavitation, J. Colloid Interface Sci. **173**, 443 (1995).

[30] C. Cottin-Bizonne, J.-L. Barrat, L. Bocquet, and E. Charlaix, Low-friction flows of liquid at nanopatterned interfaces, Nat. Mater. **2**, 237 (2003).

[31] A. Maali, Y. Pan, B. Bhushan, and E. Charlaix, Hydrodynamic drag-force measurement and slip length on microstructured surfaces, Phys. Rev. E **85**, 066310 (2012).

[32] R. S. Voronov, D. V. Papavassiliou, and L. L. Lee, Review of fluid slip over superhydrophobic surfaces and its dependence on the contact angle, Ind. Eng. Chem. Res. **47**, 2455 (2008).

[33] J. P. Rothstein, Slip on superhydrophobic surfaces, Annu. Rev. Fluid Mech. **42**, 89 (2010).

[34] R. Truesdell, A. Mammoli, P. Vorobieff, F. van Swol, and C. J. Brinker, Drag Reduction on a Patterned Superhydrophobic Surface, Phys. Rev. Lett. **97**, 044504 (2006).

[35] Y. C. Jung and B. Bhushan, Biomimetic structures for fluid drag reduction in laminar and turbulent flows, J. Phys.: Condens. Matter **22**, 035104 (2009).

[36] A. M. J. Davis and E. Lauga, Hydrodynamic friction of fakir-like superhydrophobic surfaces, J. Fluid Mech. **661**, 402 (2010).

[37] B.-Y. Cao, M. Chen, and Z.-Y. Guo, Liquid flow in surface-nanostructured channels studied by molecular dynamics simulation, Phys. Rev. E **74**, 066311 (2006).

[38] A. Steinberger, C. Cottin-Bizonne, P. Kleimann, and E. Charlaix, High friction on a bubble mattress, Nat. Mater. **6**, 665 (2007).

[39] C.-O. Ng and C. Y. Wang, Effective slip for Stokes flow over a surface patterned with two-or three-dimensional protrusions, Fluid Dyn. Res. **43**, 065504 (2011).

[40] L. Joly and T. Biben, Wetting and friction on superoleophobic surfaces, Soft Matter **5**, 2549 (2009).

[41] M. Sbragaglia and A. Prosperetti, A note on the effective slip properties for microchannel flows with ultrahydrophobic surfaces, Phys. Fluids **19**, 043603 (2007).

[42] E. Bonaccurso, H.-J. Butt, and V. S. J. Craig, Surface Roughness and Hydrodynamic Boundary Slip of a Newtonian Fluid in a Completely Wetting System, Phys. Rev. Lett. **90**, 144501 (2003).

[43] X. Dai, B. B. Stogin, S. Yang, and T.-S. Wong, Slippery Wenzel state, ACS Nano **9**, 9260 (2015).

[44] C.-O. Ng and C. Y. Wang, Apparent slip arising from Stokes shear flow over a bidimensional patterned surface, Microfluid. Nanofluid. **8**, 361 (2010).

[45] E. Lauga and H. A. Stone, Effective slip in pressure-driven Stokes flow, J. Fluid Mech. **489**, 55 (2003).

[46] E. S. Asmolov, J. Zhou, F. Schmid, and O. I. Vinogradova, Effective slip-length tensor for a flow over weakly slipping stripes, Phys. Rev. E **88**, 023004 (2013).

[47] C. Y. Wang, Flow over a surface with parallel grooves, Phys. Fluids **15**, 1114 (2003).

[48] E. S. Asmolov, S. Schmieschek, J. Harting, and O. I. Vinogradova, Flow past superhydrophobic surfaces with cosine variation in local slip length, Phys. Rev. E **87**, 023005 (2013).

[49] A. V. Belyaev and O. I. Vinogradova, Effective slip in pressure-driven flow past super-hydrophobic stripes, J. Fluid Mech. **652**, 489 (2010).

[50] E. S. Asmolov, A. V. Belyaev, and O. I. Vinogradova, Drag force on a sphere moving toward an anisotropic superhydrophobic plane, Phys. Rev. E **84**, 026330 (2011).

[51] A. D. Stroock, S. K. Dertinger, G. M. Whitesides, and A. Ajdari, Patterning flows using grooved surfaces, Anal. Chem. **74**, 5306 (2002).

[52] L. Guo, S. Chen, and M. O. Robbins, Slip boundary conditions over curved surfaces, Phys. Rev. E **93**, 013105 (2016).

[53] S. Plimpton, Fast parallel algorithms for short-range molecular dynamics, J. Comput. Phys. **117**, 1 (1995).

[54] G. S. Grest and K. Kremer, Molecular dynamics simulation for polymers in the presence of a heat bath, Phys. Rev. A **33**, 3628 (1986).

[55] R. Khare, J. J. de Pablo, and A. Yethiraj, Rheology of confined polymer melts, Macromolecules **29**, 7910 (1996).

[56] X. Yong and L. T. Zhang, Thermostats and thermostat strategies for molecular dynamics simulations of nanofluidics, J. Chem. Phys. **138**, 084503 (2013).

[57] N. Tretyakov and M. Müller, Correlation between surface topography and slippage: A molecular dynamics study, Soft Matter **9**, 3613 (2013).

[58] P. J. Hoogerbrugge and J. M. V. A. Koelman, Simulating microscopic hydrodynamic phenomena with dissipative particle dynamics, Europhys. Lett. **19**, 155 (1992).

[59] P. Espanol and P. Warren, Statistical mechanics of dissipative particle dynamics, Europhys. Lett. **30**, 191 (1995).

[60] S. Cheng and M. O. Robbins, Capillary adhesion at the nanometer scale, Phys. Rev. E **89**, 062402 (2014).

[61] R. G. Horn and J. N. Israelachvili, Direct measurement of structural forces between two surfaces in a nonpolar liquid, J. Chem. Phys. **75**, 1400 (1981).

[62] F. F. Abraham, The interfacial density profile of a Lennard-Jones fluid in contact with a (100) Lennard-Jones wall and its relationship to idealized fluid/wall systems: A Monte Carlo simulation, J. Chem. Phys. **68**, 3713 (1978).

[63] S. Toxvaerd, The structure and thermodynamics of a solid-fluid interface, J. Chem. Phys. **74**, 1998 (1981).

[64] M. Plischke and D. Henderson, Density profiles and pair correlation functions of Lennard-Jones fluids near a hard wall, J. Chem. Phys. **84**, 2846 (1986).

[65] I. Bitsanis, S. A. Somers, H. T. Davis, and M. Tirrell, Microscopic dynamics of flow in molecularly narrow pores, J. Chem. Phys. **93**, 3427 (1990).

[66] I. Bitsanis and G. Hadziioannou, Molecular dynamics simulations of the structure and dynamics of confined polymer melts, J. Chem. Phys. **92**, 3827 (1990).

[67] P. A. Thompson, M. O. Robbins, and G. S. Grest, Structure and shear response in nanometer-thick films, Isr. J. Chem. **35**, 93 (1995).

[68] J. Koplik, J. R. Banavar, and J. F. Willemsen, Molecular dynamics of fluid flow at solid surfaces, Phys. Fluids A **1**, 781 (1989).

[69] J. Koplik and J. R. Banavar, Continuum deductions from molecular hydrodynamics, Annu. Rev. Fluid Mech. **27**, 257 (1995).

[70] J. Gao, W. D. Luedtke, and U. Landman, Layering Transitions and Dynamics of Confined Liquid Films, Phys. Rev. Lett. **79**, 705 (1997).

[71] N. V. Priezjev, Shear rate threshold for the boundary slip in dense polymer films, Phys. Rev. E **80**, 031608 (2009).

[72] N. Priezjev, Relationship between induced fluid structure and boundary slip in nanoscale polymer films, Phys. Rev. E **82**, 051603 (2010).

[73] A. Niavarani and N. V. Priezjev, Slip boundary conditions for shear flow of polymer melts past atomically flat surfaces, Phys. Rev. E **77**, 041606 (2008).

[74] K. Falk, F. Sedlmeier, L. Joly, R. R. Netz, and L. Bocquet, Molecular origin of fast water transport in carbon nanotube membranes: Superlubricity versus curvature dependent friction, Nano Lett. **10**, 4067 (2010).

[75] K. Falk, F. Sedlmeier, L. Joly, R. Netz, and L. Bocquet, Ultralow liquid/solid friction in carbon nanotubes: Comprehensive theory for alcohols, alkanes, OMCTS, and water, Langmuir **28**, 14261 (2012).

[76] D. Einzel, P. Panzer, and M. Liu, Boundary Condition for Fluid Flow: Curved or Rough Surfaces, Phys. Rev. Lett. **64**, 2269 (1990).

[77] L. Bocquet and J.-L. Barrat, Hydrodynamic boundary conditions, correlation functions, and Kubo relations for confined fluids, Phys. Rev. E **49**, 3079 (1994).

[78] W. Chen, R. Zhang, and J. Koplik, Velocity slip on curved surfaces, Phys. Rev. E **89**, 023005 (2014).

[79] N. V. Priezjev, Molecular diffusion and slip boundary conditions at smooth surfaces with periodic and random nanoscale textures, J. Chem. Phys. **135**, 204704 (2011).

[80] M. Z. Bazant and O. I. Vinogradova, Tensorial hydrodynamic slip, J. Fluid Mech. **613**, 125 (2008).

[81] C. Y. Soong, T. H. Yen, and P. Y. Tzeng, Molecular dynamics simulation of nanochannel flows with effects of wall lattice-fluid interactions, Phys. Rev. E **76**, 036303 (2007).

[82] N. V. Priezjev and S. M. Troian, Molecular Origin and Dynamic Behavior of Slip in Sheared Polymer Films, Phys. Rev. Lett. **92**, 018302 (2004).

[83] L. M. Hocking, A moving fluid interface on a rough surface, J. Fluid Mech. **76**, 801 (1976).

[84] S. Richardson, On the no-slip boundary condition, J. Fluid Mech. **59**, 707 (1973).

[85] E. O. Tuck and A. Kouzoubov, A laminar roughness boundary condition, J. Fluid Mech. **300**, 59 (1995).

[86] D. W. Bechert and M. Bartenwerfer, The viscous flow on surfaces with longitudinal ribs, J. Fluid Mech. **206**, 105 (1989).

[87] K. M. Jansons, Determination of the macroscopic (partial) slip boundary condition for a viscous flow over a randomly rough surface with a perfect slip microscopic boundary condition, Phys. Fluids **31**, 15 (1988).

[88] C. Pozrikidis, Creeping flow in two-dimensional channels, J. Fluid Mech. **180**, 495 (1987).

[89] M. Cieplak, E. D. Smith, and M. O. Robbins, Molecular origins of friction: The force on adsorbed layers, Science **265**, 1209 (1994).

[90] E. D. Smith, M. O. Robbins, and M. Cieplak, Friction on adsorbed monolayers, Phys. Rev. B **54**, 8252 (1996).

[91] M. O. Robbins and M. H. Müser, Computer simulations of friction, lubrication and water, in *Modern Tribology Handbook*, edited by B. Bhushan (CRC Press, Boca Raton, 2001), p. 717.